Supporting Information

Cross-linked nanoflower network and Se-doping enabling sulfur rich SPAN towards lithium–sulfur batteries beyond 600 Wh kg^{-1}

Qiang Wu[a], Yuanke Wu[ab], Hui Yan[c], Wei Zhong[ab], Mingsheng Qin[ab], Haolin Zhu[a], Shijie Cheng[a], Jia Xie*[a]

[a] State Key Laboratory of Advanced Electromagnetic Technology, School of Electrical and Electronic Engineering, Huazhong University of Science and Technology, Wuhan, Hubei, 430074, P. R. China

[b] State Key Laboratory of Materials Processing and Die & Mould Technology, School of Materials Science and Engineering, Huazhong University of Science and Technology, Wuhan, Hubei, 430074, P. R. China

[c] Institute of Metal Research, Chinese Academy of Sciences, Shenyang, Liaoning, 110016, P. R. China

Corresponding authors:

E-mail: xiejia@hust.edu.cn (Jia Xie)

Experimental

Chemicals: Acrylonitrile (AN), 2,2'-Azobis(2-methylpropionitrile) (AIBN), ethylene glycol dimethyl ether (DME), carboxymethyl cellulose (CMC-Na) and Selenium (Se) were obtained from Shanghai Aladdin Biochemical Technology Co., Ltd. Hydrazine hydrate and acetone (AT) was supplied by Sinopharm Chemical Reagent Co., Ltd. Lithium bis(fluorosulfonyl)imide (LiFSI) was purchased form DoDoChem. Tetrafluoroethyl 2,2,3,3-tetrafluoropropyl ether (TTE) was acquired from Shandong Binlaichem Pharmaceutical Co., Ltd. Styrene butadiene rubber (SBR) and Ketjen black (KB, ECP-600JD) were purchased from Guangdong Canrd New Energy Technology Co. Ltd. Sulfur (S) powder was obtained from Sigma-Aldrich.

Synthesis of FPAN: Flower-liked polyacrylonitrile (FPAN) was prepared by in-situ polymerization[1]. Specifically, we initially introduced 15 mL of AN into the round-bottomed flask, followed by adding 15 mL AT. Subsequently, we incorporated 15 mg AIBN as an initiator and heated it under nitrogen atmosphere at 70 °C for 2 hours, resulting in the formation of a white solid powder and termination of the reaction. After the reaction was complete, the white powders were collected and fully dried in vacuum oven (70 °C, 12 h) to obtain the final flower-like polyacrylonitrile (FPAN).

Synthesis of NH-FPAN: Firstly, the crosslinking reaction solution of anhydrous ethanol and hydrazine hydrate was prepared in a volume ratio of 3:1 (v/v). Subsequently, the prepared white FPAN powder was added to the solution and heated in an oil bath at 70 °C. The color of the powder transitioned from white to yellow, indicating completion of the reaction after 8 hours. Following this, the yellow powder was subjected to three rounds of deionized water washing for solvent removal before being collected through filtration. Finally, vacuum oven drying at 70 °C for 24 hours yielded the desired product (NH-FPAN).

Synthesis of $FSe_{0.04}S_{0.96}PAN$ and $NH\text{-}FSe_{0.03}S_{0.97}PAN$composites: FPAN/NH-FPAN and Se_xS_{1-x} powder (The Se_xS_{1-x} powder was prepared by heat treatment of Se and S sealed tubes with mass ratio of 1:15.) were mixed in a weight ratio of 1:3 and ground in mortar for 1 h until homogeneously dispersed. The uniform mixture was poured into a porcelain boat and further heated at 80 °C for 1 h and 300 °C for 2.5 h in argon (Ar) atmosphere. The final products were denoted as $FSe_{0.04}S_{0.96}PAN$ and NH-$FSe_{0.03}S_{0.97}PAN$, respectively.

Preparation of sulfur cathode: *D*eionized water was served as solvent, and slurry was generated by blending 80 wt% $FSe_{0.04}S_{0.96}PAN$ or NH-$FSe_{0.03}S_{0.97}PAN$, 10 wt% KB, 5 wt% CMC-Na and 5 wt% SBR in a slurry homogenizer. Then the slurry was casted on the carbon-coated aluminum foil and dried at 70 °C for 12 h. The cathode loading was about 2 mg cm^{-2}. Additionally, the high loading NH-$FSe_{0.03}S_{0.97}PAN$ slurry was generated by blending 85 wt% NH-$FSe_{0.03}S_{0.97}PAN$, 7.5 wt% KB, 3.75% CMC-Na and 3.75 wt% SBR in a slurry homogenizer. The electrode loadings were about 7.4, 16.0 and 24.0 mg cm^{-2}.

Electrochemical Measurements: The CR2032 coin-cells were assembled in a glove box filled with argon gas (H_2O and O_2 < 0.1 ppm). $FSe_{0.04}S_{0.96}PAN$/NH-$FSe_{0.03}S_{0.97}PAN$ was used as the cathode, while Li foil served as the anode, and PP was utilized as the separator. LiFSI: DME: TTE = 1: 1.2: 1 (molar ratio) were adopted as the electrolyte and 40 μL electrolyte was added to cells. In addition, the coin-cell and pouch-cell were tested under practical conditions, and the cathode loading was 7.4, 16.0, 24.0 mg cm^{-2}, respectively. The Li−S batteries galvanostatic discharge-charge experiments were measured by the Neware electrochemical testing system. The electrochemical workstation (Solartron 1470E) was used to test cyclic voltammetry (CV) profiles at various scan rates of 0.1-0.5 mV s^{-1} between 1 and 3 V in Li−S batteries. Li^+ ion diffusion coefficients for $FSe_{0.04}S_{0.96}PAN$ or NH-$FSe_{0.03}S_{0.97}PAN$ samples were calculated by a series of cyclic voltammograms with different scan rates, and the results were analyzed based on Randles-Sevick equation: $I_p = 2.69 \times 10^5\ n^{1.5}\ A\ D_{Li+}^{0.5}\ C_{Li+}\ v^{0.5}$, in which Ip represented the peak current (A), D_{Li+} stood for lithium ion diffusion coefficient (cm^2 s^{-1}), n was the number of electrons involved in the reaction (n = 2 for Li−S battery), A referred to the geometric area of the active electrode (cm^2), C_{Li+} represented the Li ion concentration (mol L^{-1}) and ν stands for scanning rate (V s^{-1}). The Galvanostatic intermittent titration technique (GITT) test was conducted by discharging or charging batteries at a current density of 0.1C for 1 h, followed by a resting period of 4 h. The diffusion coefficicnt (D_{Li+}) from GITT is calculated as the following Equation:

$$D = \frac{4}{\pi\tau}\left(\frac{m_B V_M}{M_B S}\right)^2\left(\frac{\Delta E_S}{\Delta E_\tau}\right)^2$$

Where τ is the duration of the current impulse, m_B is the mass loading of the active material, S represents the electrode area, ΔE_S is the quasi-thermodynamic equilibrium potential difference between before and after the current pulse, ΔE_τ represents the potential difference during the current pulse; V_M is the molar volume of the active materials, and M_B is the molar mass of active material.

Material characterizations: X-ray diffraction (XRD) patterns were obtained using a diffractomete (PANalytical X'Pert PRODY2198, Holland), with Cu Kα radiation (40 kV, 100 mA, λ = 1.54056 Å). Elemental analysis was performed on CHN and CHNS elemental analyzers (Vario Micro cube, Elementar). Raman spectra were performed by LabRAM HR800 (Horiba Jobin Yvon) with laser power 5 mW, wavelength 532 nm and exposure time 10 s. Fourier transform infrared spectra (FT-IR) was taken using a Bruker Vertex 70 FT-IR spectrometer. The Brunauer-Emmett-Teller (BET) surface area was calculated using the adsorption data. The morphologies of the samples were investigated by scanning electron microscopy (SEM, TESCAN MIRA LMS). Transmission electron microscopy (TEM) was carried out with a Tecnai G2 F30 (FEI, Holland) instrument, equipped with an X-ray energy dispersive spectrometer (EDS). The surface chemical compositions of powders ($FSe_{0.04}S_{0.96}PAN$ or NH-$FSe_{0.03}S_{0.97}PAN$) were analyzed by X-ray photoelectron spectrometry (XPS) (Thermo Scientific ESCALAB Xi+).

Calculation method: The Density functional theory (DFT) calculations were performed by using the Vienna ab-initio Simulation Package (VASP). The generalized gradient approximation (GGA) of the Perdew-Burke-Ernzerhof (PBE) functional is used to describe the exchange-correlation energy, while the projector augmented wave (PAW) potential was employed to represent the interactions of electrons with ion cores. The plane wave cutoff energy was set to 400 eV, and a Monkhorst-Pack 3 × 3 × 1 k-point mesh was used for Brillouin zone sampling. The convergence criteria of energy and force were set to 10^{-5} eV and 0.02 eV Å^{-1}, respectively. A monolayer graphene with a supercell size of 5 × 5 was nitrogen-doped. The vacuum thickness in the z direction is set to 20 Å for erasing the effect of periodic condition for slab model. The adsorption energy between the slab and different sulfur molecules was calculated as following equation:

$$E_a = E_{total} - E_{slab} - E_{mol}$$

in which E_{total} is the total energy of the adsorption system, E_{slab} and E_{mol} are the energy of different nitrogen-doped graphene and polysulfide molecules, respectively.

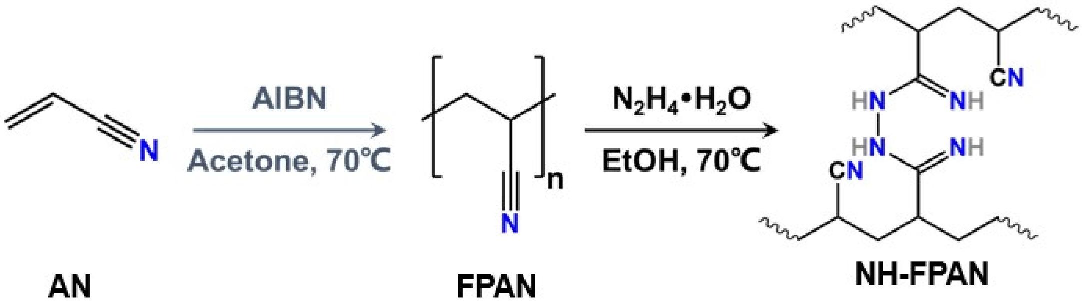

Fig. S1. Synthetic reaction mechanism of FPAN and NH-FPAN materials.

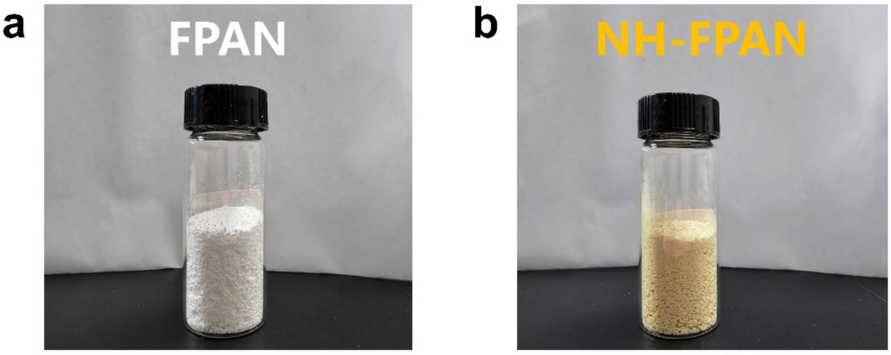

Fig. S2. The optical photographs of (a) FPAN and (b) NH-FPAN materials.

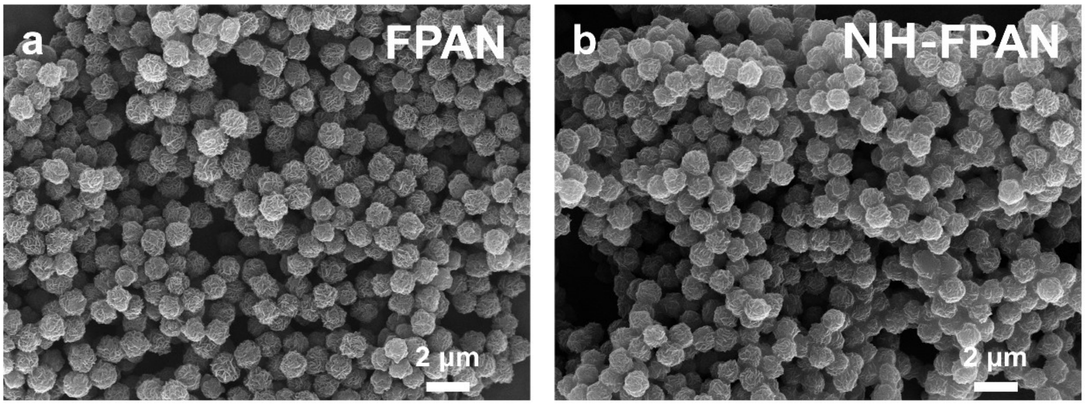

Fig. S3. The low-magnification SEM images of (a) FPAN and (b) NH-FPAN.

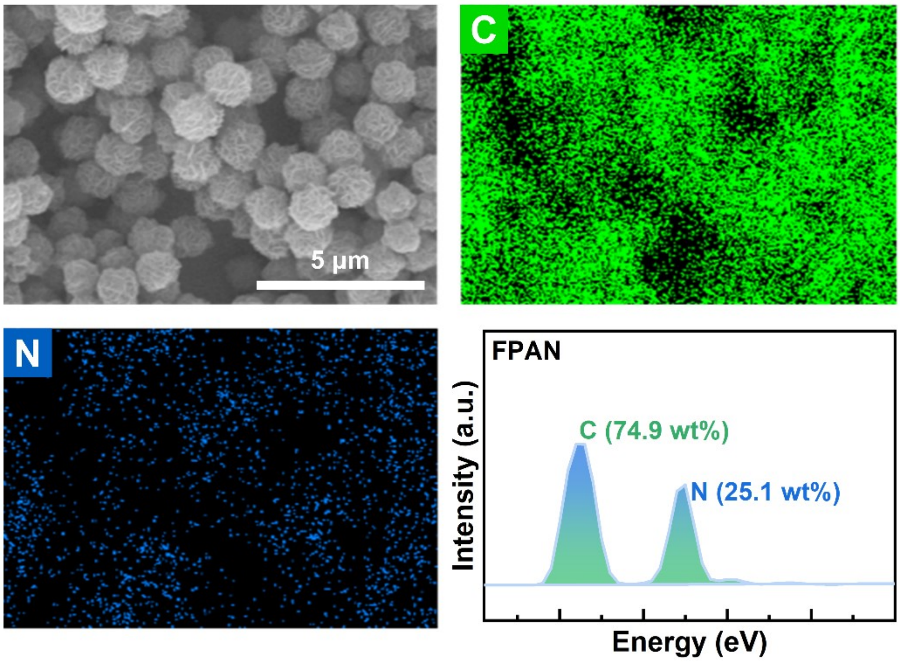

Fig. S4. The SEM images and corresponding element mapping of FPAN.

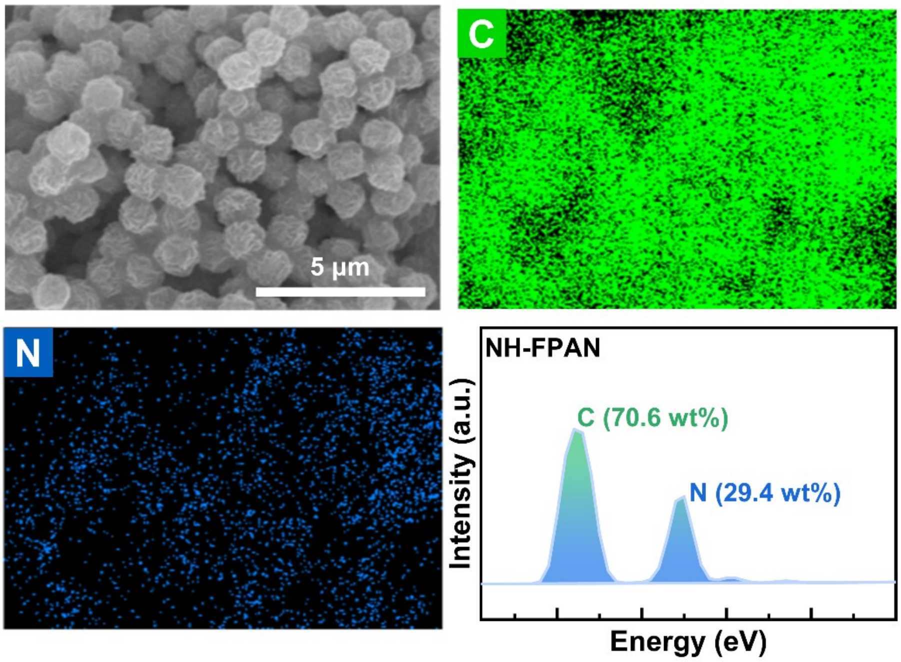

Fig. S5. The SEM images and corresponding element mapping of NH-FPAN.

Table S1. The element analysis of FPAN and NH-FPAN precursors.

Materials	C (%)	N (%)	H (%)
FPAN	67.5	26.0	5.7
NH-FPAN	65.1	29.3	5.2

Table S2. The element analysis of $FSe_{0.04}S_{0.96}PAN$ and NH-$FSe_{0.03}S_{0.97}PAN$ composites.

Materials	C (%)	N (%)	H (%)	S (%)	Se (%)	S&Se (%)
$FSe_{0.04}S_{0.96}PAN$	27.9	9.9	0.8	55.3	6.1	61.4
NH-$FSe_{0.03}S_{0.97}PAN$	25.1	9.1	0.5	60.1	5.2	65.3

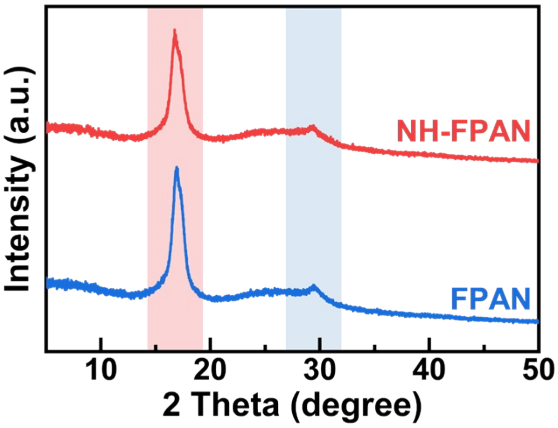

Fig. S6. The XRD pattern of FPAN and NH-FPAN.

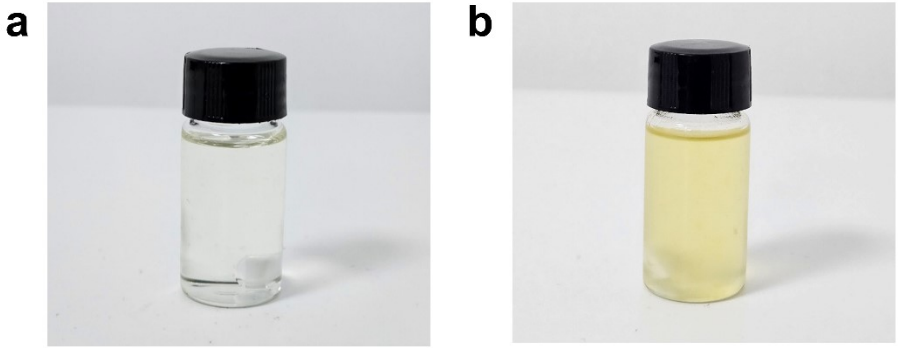

Fig. S7. The optical photographs of (a) FPAN and (b) NH-FPAN in DMF.

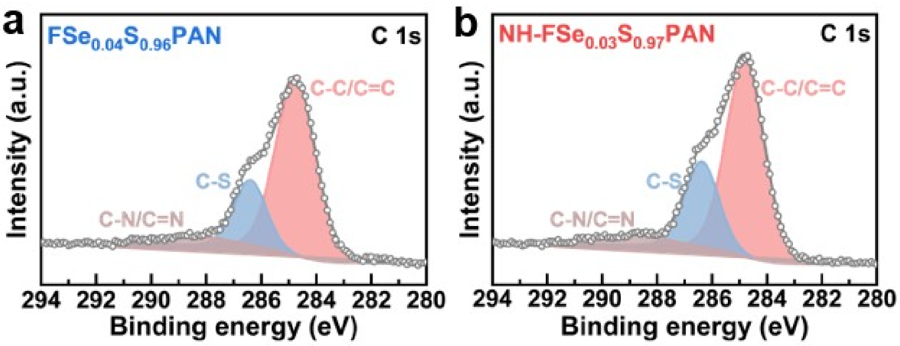

Fig. S8. The C 1s spectra of (a) $FSe_{0.04}S_{0.96}PAN$ and (b) $NH\text{-}FSe_{0.03}S_{0.97}PAN$ composites, respectively.

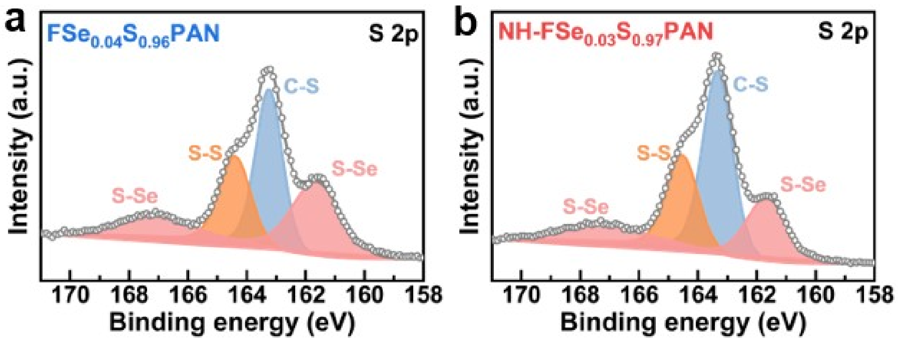

Fig. S9. The S 2p spectra of (a) $FSe_{0.04}S_{0.96}PAN$ and (b) $NH\text{-}FSe_{0.03}S_{0.97}PAN$ composites, respectively.

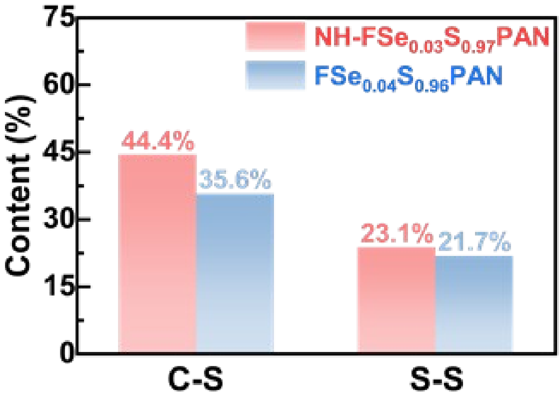

Fig. S10. Corresponding content of C–S and S–S bonds in the $FSe_{0.04}S_{0.96}PAN$ and NH-$FSe_{0.03}S_{0.97}PAN$.

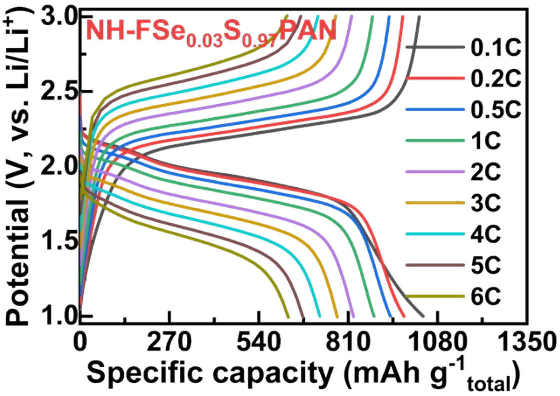

Fig. S11. The discharge-charge curves of NH-$FSe_{0.03}S_{0.97}PAN$ at different rates.

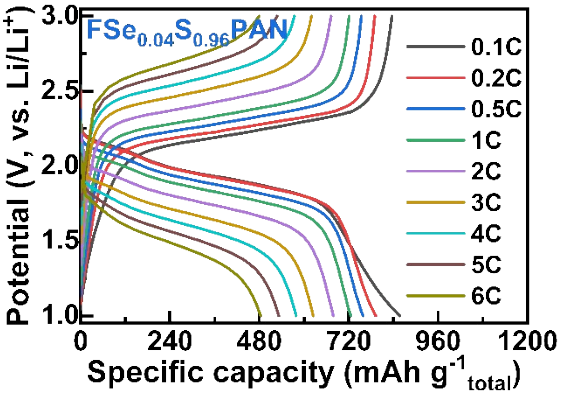

Fig. S12. The discharge-charge curves of $FSe_{0.04}S_{0.96}PAN$ at different rates.

Table S3. A comparison of Li–S battery performances between the NH-$FSe_{0.03}S_{0.97}PAN$ and recently reported advanced SPAN-based composites and high sulfur content composites.

Material	Active material content (%)	Composite reversible capacity (mAh g^{-1})	Utilization rate (%)	Ref.
S@PAN/S_7Se	68.0	723	64.9	1
MoS_2@SPAN	44.9	626	83.2%	2
SPAN@D-KB	45.7	700	91.5	3
MCS-FSPAN	45.0	601	79.8	4
S-HYB	62.0	903	87.0	5
S@Co−N/G	90.0	1089	72.2	6
G-g-sPS@S	96.0	1026	63.8	7
S/FeCo-SACC	78.4	1026	78.1	8
STI	90.0	1011	67.1	9
S@Co-C-CNTs	80.0	936	69.9	10
NH-$FSe_{0.03}S_{0.97}PAN$	65.3	1036	97.9	This work

Table S4. A comparison of Li–S battery performances between the NH-$FSe_{0.03}S_{0.97}PAN$ and recently reported state-of-the-art cathode materials at 1C.

Material	Active material content (%)	Composite reversible capacity (mAh g^{-1})	Cycle number (n)	Capacity decay (per cycle)	Ref.
$NiS_2/NiSe_2$@NC/S	73.8	664	500	0.026%	[11]
S/BVO/CNT	80.1	752	500	0.050%	[12]
CNT/NS@PEDOT	68.3	627	1000	0.011%	[13]
S/Co-MnO@CF	63	500	400	0.058%	[14]
S@NiS_4-TAPT	77	714	400	0.075%	[15]
MXene-ZnI_2/S	70	595	1000	0.042%	[16]
v-ZnTe/$CoTe_2$@NC/S	68	612	500	0.034%	[17]
Fe_3O_4/FeP@C-S	70	765	300	0.127%	[18]
S-Vo-BOC/rGO	70	647	1500	0.031%	[19]
NH-$FSe_{0.03}S_{0.97}PAN$	65.3	971	1200	0.017%	This work

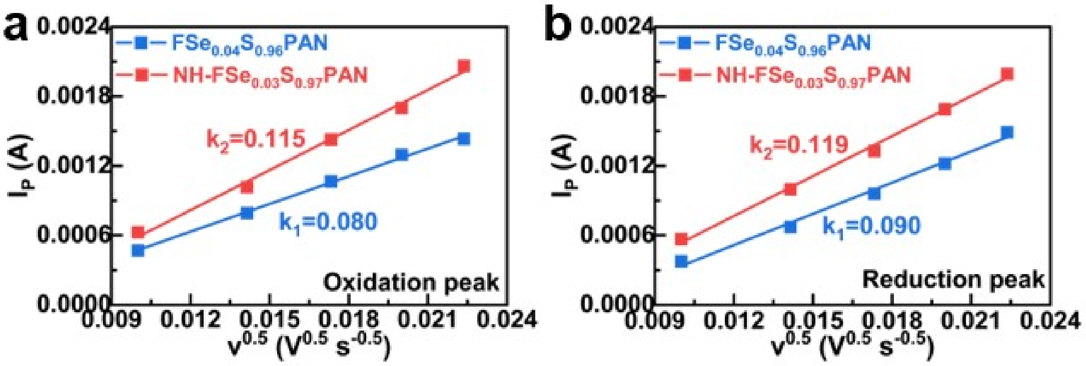

Fig. S13. Peak current versus square root of scan rate plots for the (a) oxidation process and (b) reduction processes of Li–S batteries.

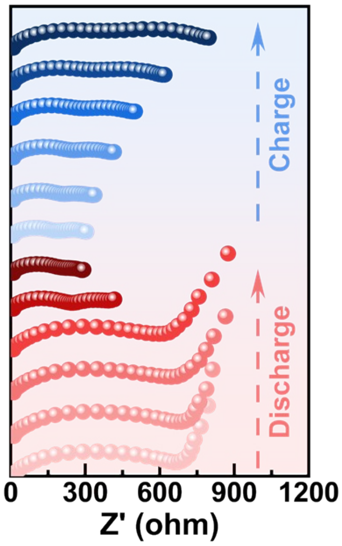

Fig. S14. Impedance spectra of $FSe_{0.04}S_{0.96}PAN$ during first cycle.

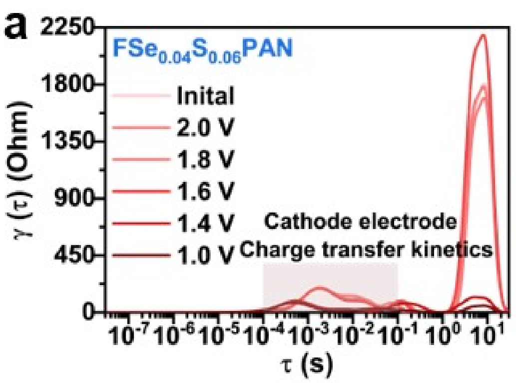

Fig. S15. Combined DRT profiles of (a) $FSe_{0.04}S_{0.96}PAN$ and (b) NH-$FSe_{0.03}S_{0.97}PAN$ during discharge.

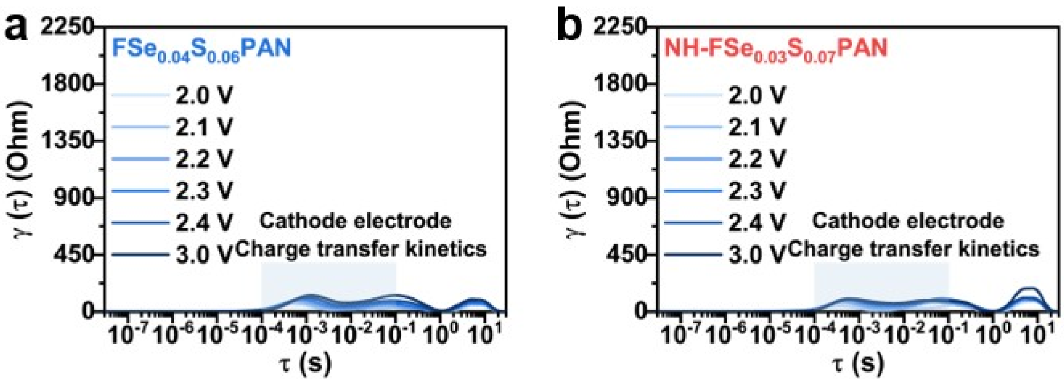

Fig. S16. Combined DRT profiles of (a) $FSe_{0.04}S_{0.96}PAN$ and (b) NH-$FSe_{0.03}S_{0.97}PAN$ during discharge.

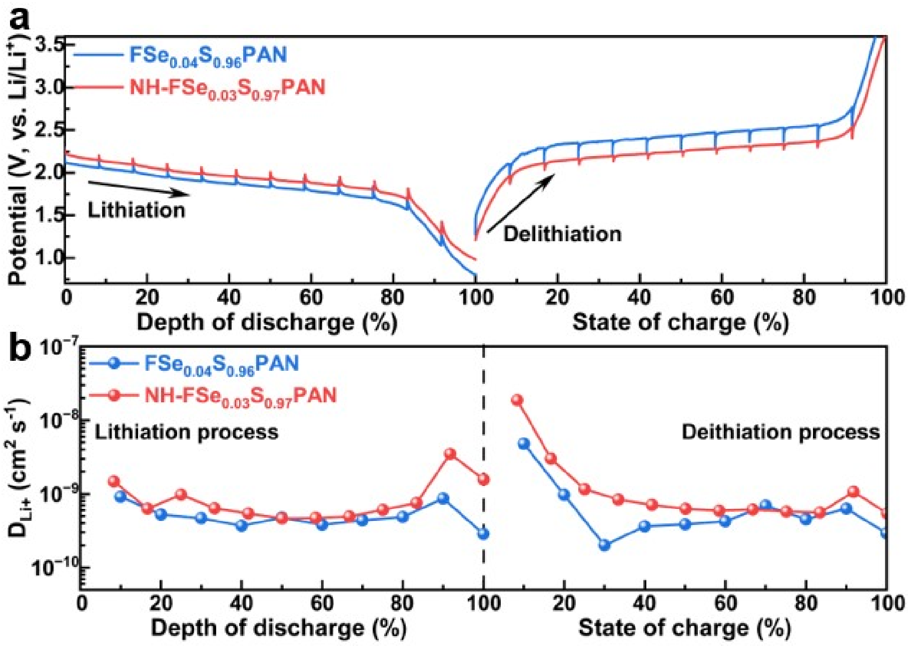

Fig. 17. Voltage profiles (a) and the Li^+ diffusion coefficients (b) of $FSe_{0.04}S_{0.96}PAN$ and NH-$FSe_{0.03}S_{0.97}PAN$ obtained via the GITT technique during discharge-charge processes.

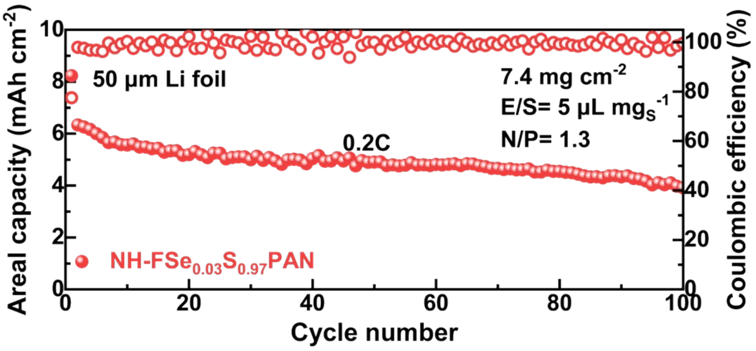

Fig. S18. Cycling performance of NH-$FSe_{0.03}S_{0.97}PAN$ at 0.2C under practical conditions (loading: 7.4 mg cm^{-2}, E/S=5 μL mg_S^{-1}, N/P=1.3).

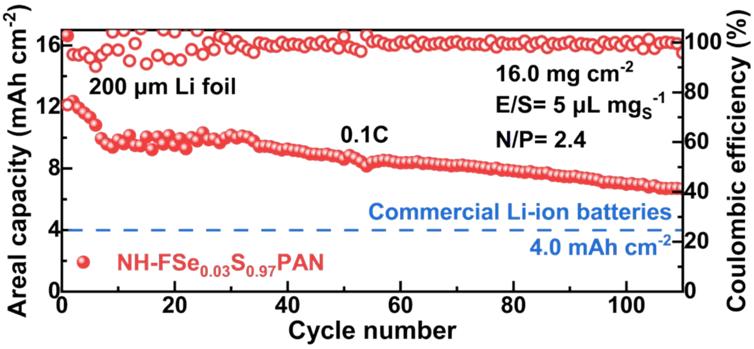

Fig. S19. Cycling performance of NH-FSe$_{0.03}$S$_{0.97}$PAN under practical conditions (loading: 16.0 mg cm^{-2}, E/S=5 μL mg$_S^{-1}$, N/P=2.4).

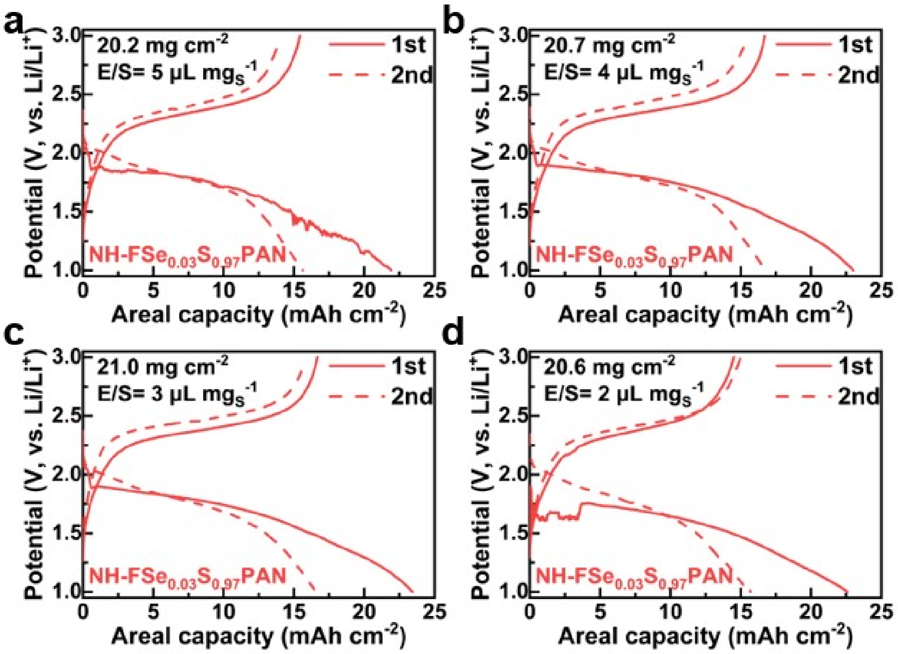

Fig. S20. Discharge-charge curves of Li–S batteries at different E/S ratios.

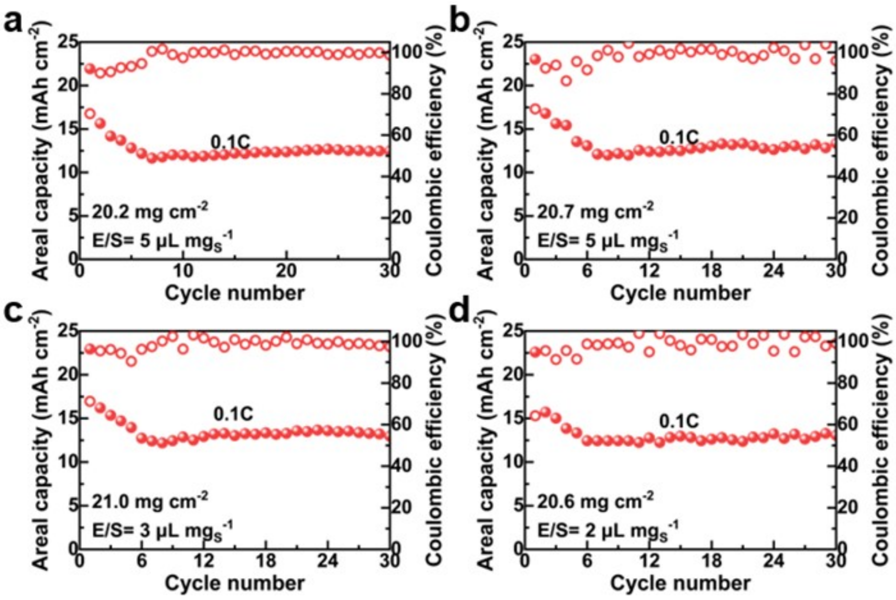

Fig. S21. Cycling performance of Li–S batteries at different E/S ratios.

Table S5. Estimated gravimetric energy density of Li−S coin batteries.

Initial area energy (mWh cm^{-2})		43.3
Reversible area energy (mWh cm^{-2})		34.6
Areal loading (mg cm^{-2})	NH-FSe$_{0.03}$S$_{0.97}$PAN cathode	24.8
	Li foil (200 μm)	10.4
	Al foil (8 μm)	1.8
	Separator (20 μm)	0.9
	Electrolyte	29.9
Initial and reversible cycled energy density (based on based total materials, Wh kg^{-1})		638.6/510.3

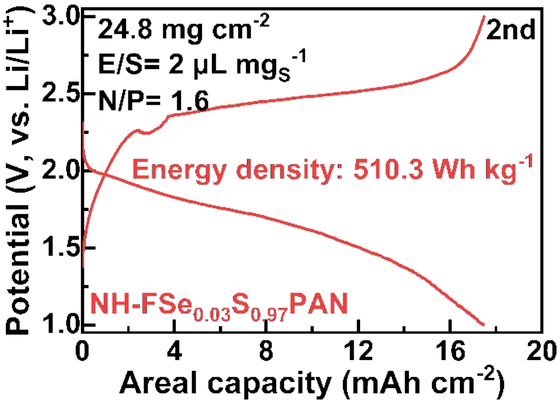

Fig. S22. The second discharge-charge curve of NH-$FSe_{0.03}S_{0.97}$PAN under practical conditions (loading: 24.8 mg cm^{-2}, E/S=2 μL $mg_S{}^{-1}$, N/P=1.6).

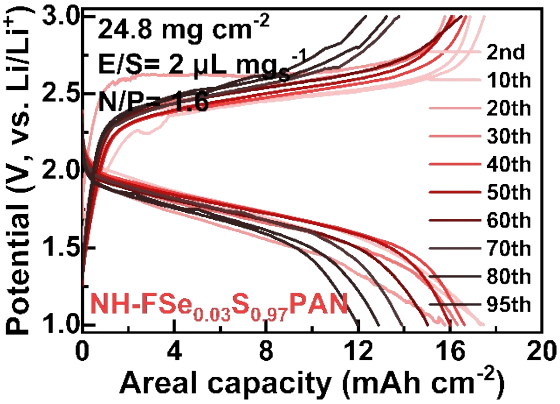

Fig. S23. The discharge-charge curve of NH-$FSe_{0.03}S_{0.97}$PAN at different cycles under practical conditions (loading: 24.8 mg cm^{-2}, E/S=2 μL $mg_S{}^{-1}$, N/P=1.6).

Table S6. A comparison of Li–S battery performances between the NH-$FSe_{0.03}S_{0.97}PAN$ and recently reported state-of-the-art cathode materials.

Material	Areal loading (mg_S cm^{-2})	Areal capacity (mAh cm^{-2})	N/P	E/S (μL mg^{-1})	Cycle number	Ref.
Mo_2C@LCS/S	11.2	6	N/A	N/A	100	[20]
S@Co-SAs/C_2N	8.1	7	N/A	4.7	100	[21]
HE-MXene/S	5.4	5	N/A	N/A	100	[22]
S/HEA@HC/HCNB	9.0	10	N/A	10	35	[23]
CF-SCNT-HrGO	9.0	13	N/A	N/A	30	[24]
S@CoSA-N_3PS	6.0	4	N/A	N/A	60	[25]
NH-$FSe_{0.03}S_{0.97}PAN$	16.1	17.6	1.6	2	120	This work

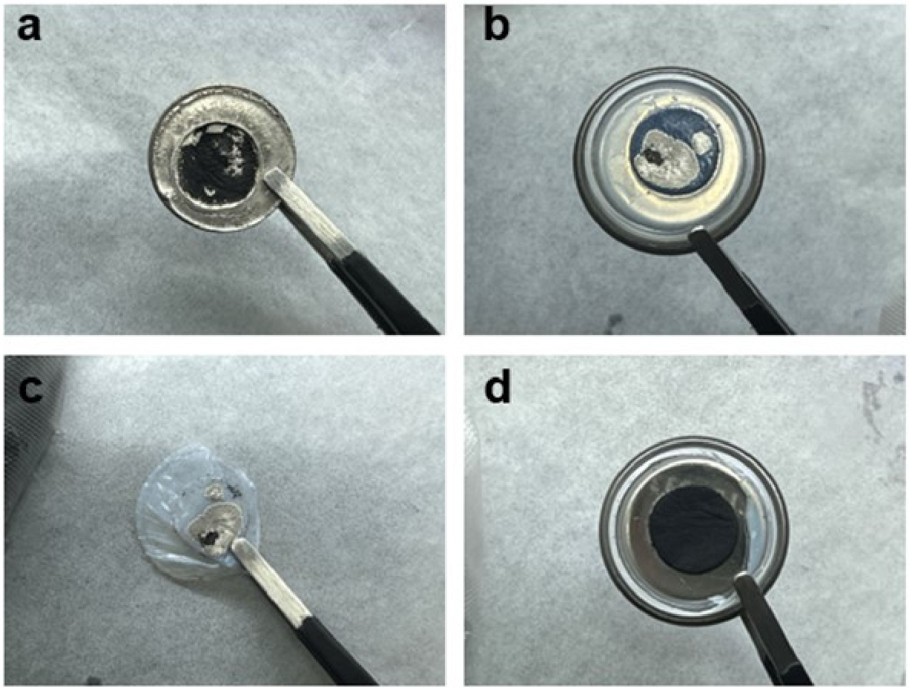

Fig. S24. Optical images of (a) lithium metal anode, (b) separator and cathode, (c) separator and (d) NH-FSe$_{0.03}$S$_{0.97}$PAN electrode after 120 cycles under harsh conditions.

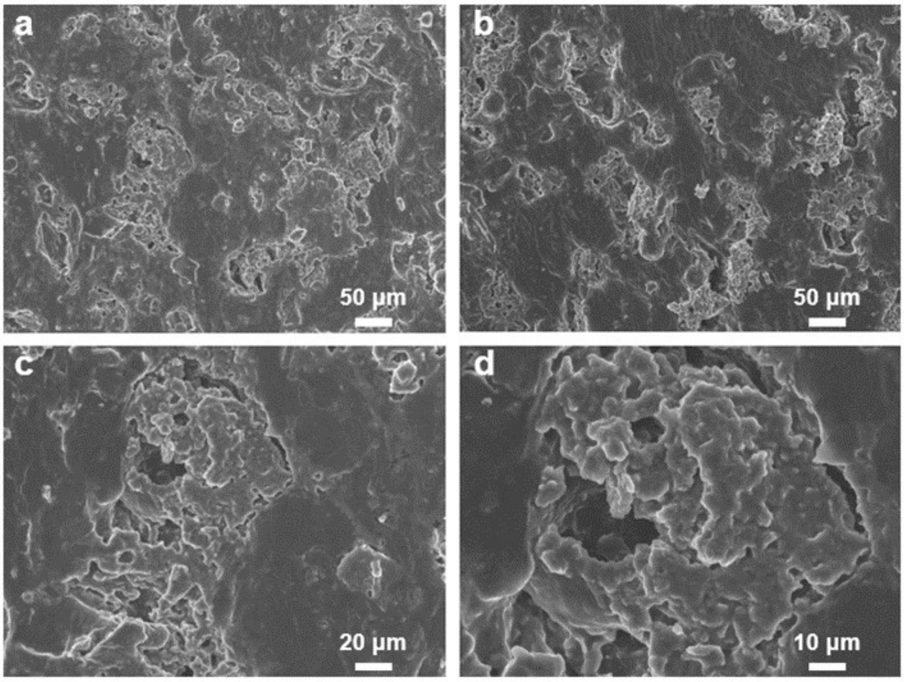

Fig. S25. (a-b) SEM images of lithium metal anode at different magnification after 120 cycles under harsh conditions.

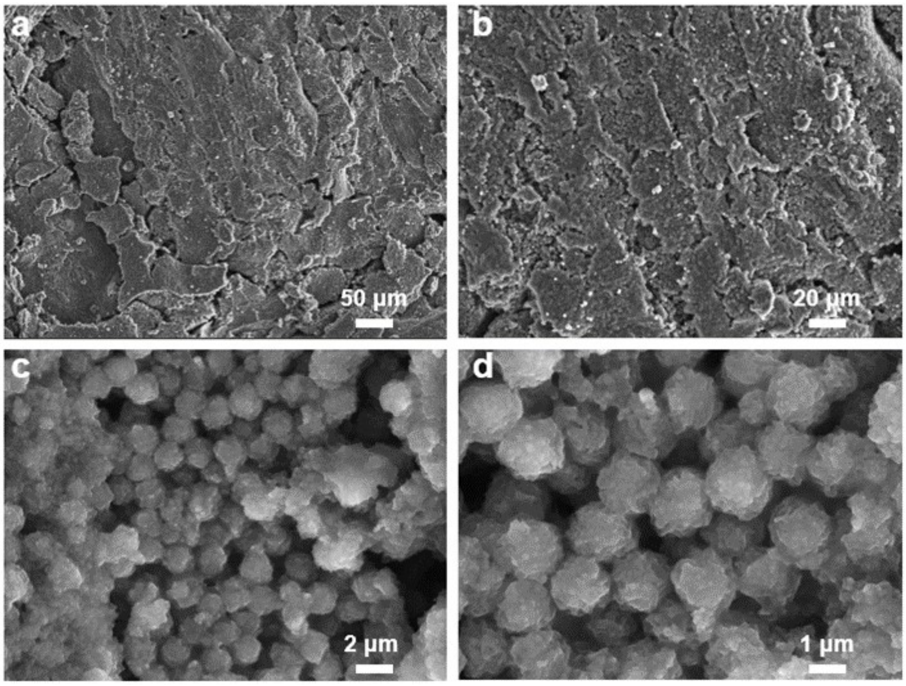

Fig. S26. (a-b) SEM images of NH-FSe$_{0.03}$S$_{0.97}$PAN electrode at different magnification after 120 cycles under harsh conditions.

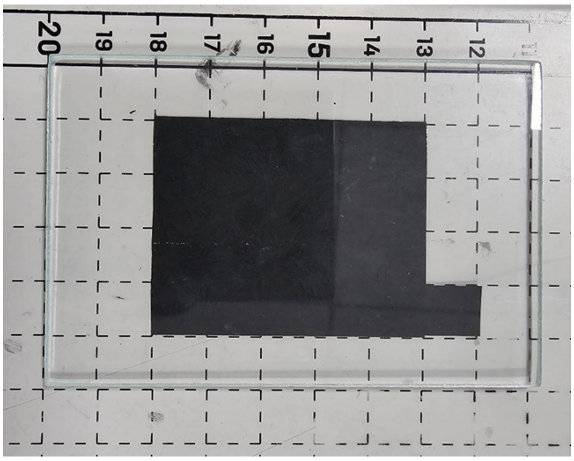

Fig. S27. The optical photographs of NH-FSe$_{0.03}$S$_{0.97}$PAN electrode (4 × 5 cm^2) for pouch cell.

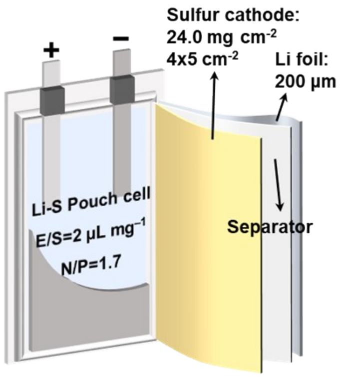

Fig. S28. Configuration of Li−S pouch cell.

Table S7. Estimated gravimetric energy density of Li−S pouch batteries.

Initial area energy(mWh cm^{-2})		36.7
Reversible area energy (mWh cm^{-2})		33.7
Areal loading (mg cm^{-2})	NH-F$Se_{0.03}S_{0.97}$PAN cathode	24.0
	Li foil (200 μm)	10.4
	Al foil (8 μm)	1.8
	Separator (20 μm)	0.9
	Electrolyte	29.0
Initial and reversible cycled energy density (based on cathode and anode, Wh kg^{-1})		555.2/509.8

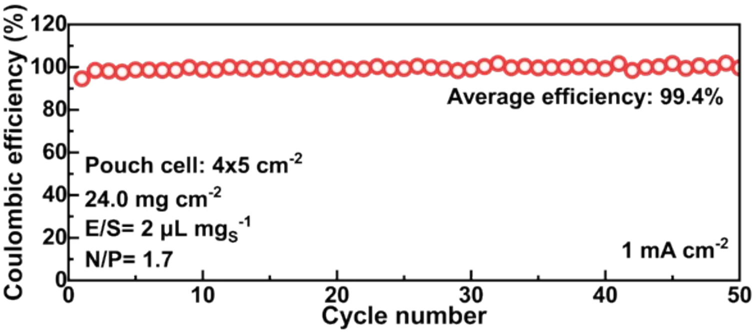

Fig. S29. Coulombic efficiency of Li−S pouch cell under practical conditions.

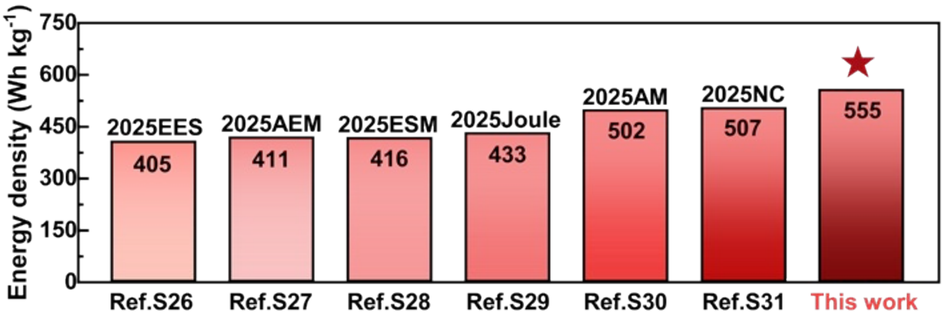

Fig. S30. Energy density comparison between this work and previously reported Li−S pouch cells (based on the total battery materials, excluding packaging).

References

1. B. He, Z. Rao, Z. Cheng, D. Liu, D. He, J. Chen, Z. Miao, L. Yuan, Z. Li and Y. Huang, *Adv. Energy Mater.*, 2021, **11**, 2003690.
2. L. Wang, H. Shi, Y. Xie and Z.-S. Wu, *Carbon neutraliz.*, 2023, **2**, 262-270.
3. A. Xu, Z. Jin, B. Wang, X. Xie, X. Xiao, A. Wang, J. Zhang, W. Wang, J. Lu and F. Zeng, *Chem. Eng. J.*, 2024, **484**, 149558.
4. J. Wang, X. Zhao, Q. Zou and M. Wei, *J. Mater. Chem. A*, 2025, **13**, 4150-4158.
5. M. Liao, Y. Xu, M. M. Rahman, S. Tan, D. Wang, K. Wang, N. K. Dandu, Q. Lu, G. Li, L. Le, R. Kou, H. Jiang, A. Nguyen, P. Shi, L. Ye, A. T. Ngo, E. Hu, C. Wang and D. Wang, *Nat. Sustain.*, 2024, **7**, 1709-1718.
6. Z. Du, X. Chen, W. Hu, C. Chuang, S. Xie, A. Hu, W. Yan, X. Kong, X. Wu, H. Ji and L.-J. Wan, *J. Am. Chem. Soc.*, 2019, **141**, 3977-3985.
7. J. Wu, J. Huang, Y. Cui, D. Miao, X. Ke, Y. Lu and D. Wu, *Adv. Mater.*, 2023, **35**, 2211471.
8. X. Wang, X. Zhang, Y. Zhang, J. Wang, J. Liu, S. Li, X. Liu, M. Jin, L. Zhao, G. Li and X. Wang, *Adv. Energy Mater.*, 2024, **14**, 2400926.
9. X. Li, L. Yuan, D. Liu, Z. Li, J. Chen, K. Yuan, J. Xiang and Y. Huang, *Energy Stor. Mater.*, 2020, **26**, 570-576.
10. Y. Xiang, F. Yan, Z. Zhao, J. Li, W. Li, W. Zhang, L. Lu and Y. Pei, *J Colloid Interf Sci*, 2024, **674**, 959-971.
11. C. Huang, J. Yu, C. Y. Zhang, Z. Cui, J. Chen, W.-H. Lai, Y.-J. Lei, B. Nan, X. Lu, R. He, L. Gong, J. Li, C. Li, X. Qi, Q. Xue, J. Y. Zhou, X. Qi, L. Balcells, J. Arbiol and A. Cabot, *Adv. Mater.*, 2024, **36**, 2400810.
12. A. Huang, L. Kong, B. Zhang, X. Liu, L. Wang, L. Li and J. Xu, *ACS Nano*, 2024, **18**, 12795-12807.
13. B. Wang, Y. Wang, Y. Lan, G. Lu, L. Liu, T. Tang, M. Li, Y. Cheng, J. Xiao and X. Li, *Angew. Chem., Int. Ed.*, 2024, **63**, e202406693.
14. H. Zhu, S. Chen, X. Yao, K. Yang, W. Zhao, T. Chen, L. Yang and F. Pan, *Adv. Funct. Mater.*, 2024, **34**, 2401470.
15. S. Lv, X. Ma, S. Ke, Y. Wang, T. Ma, S. Yuan, Z. Jin and J.-L. Zuo, *J.Am.Chem.Soc.*, 2024, **146**, 9385-9394.
16. L. Peng, J. Han, Y. Cao, C. Geng, Z.-Z. Pan, H. Nishihara, Q.-H. Yang and W. Lv, *Adv. Funct. Mater*, 2024, **34**, 2310508.
17. C. Huang, J. Yu, C. Li, Z. Cui, C. Zhang, C. Zhang, B. Nan, J. Li, J. Arbiol and A. Cabot, *Adv. Funct. Mater*, 2023, **33**, 2305624.
18. J. Li, Z. Wang, K. Shi, Y. Wu, W. Huang, Y. Min, Q. Liu and Z. Liang, *Adv. Energy Mater.*, 2024, **14**, 2303546.
19. C. Zhao, B. Jiang, Y. Huang, X. Sun, M. Wang, Y. Zhang and N. Zhang, *Energy Environ. Sci.*, 2023, **16**, 5490-5499.
20. H. Yuan, J. Zheng, G. Lu, L. Zhang, T. Yan, J. Luo, Y. Wang, Y. Liu, T. Guo, Z. Wang, J. Nai and X. Tao, *Adv. Mater.*, 2024, **36**, 2400639.
21. D. Yang, J. Wang, C. Lou, M. Li, C. Zhang, A. Ramon, C. Li, M. Tang, G.

Henkelman, M. Xu, J. Li, J. Llorca, J. Arbiol, D. Mitlin, G. Zhou and A. Cabot, *ACS Energy Lett.*, 2024, **9**, 2083-2091.

22. M. Xu, Q. Zhu, Y. Li, Y. Gao, N. Sun and B. Xu, *Energy Environ. Sci.*, 2024, **17**, 7735-7748.
23. F. Han, Z. Wang, Q. Jin, L. Fan, K. Tao, L. Li, L. Shi, H.-Q. Lu, Z. Zhang, J. Li, X. Zhang and L. Wu, *ACS Nano*, 2024, **18**, 15167-15176.
24. Q. Guo, C. Wang, J. Shang, Y. Yang, C. Xie, Y. Luo, M. Rong, Y. Pei, Y. Gao and Z. Zheng, *Adv. Mater.*, 2024, **36**, 2400041.
25. C. Dong, C. Ma, C. Zhou, Y. Yu, J. Wang, K. Yu, C. Shen, J. Gu, K. Yan, A. Zheng, M. Gong, X. Xu and L. Mai, *Adv. Mater.*, 2024, **36**, 2407070.
26. X. Jiao, L. Tan, X. Tang, C. Tong, T. Wang, M. Shao, B. Liu, C. Li and Z. Wei, *Energy Environ. Sci.,*, 2025, DOI: 10.1039/D5EE00615E.
27. M. Li, H. Liu, Z. Cheng, J. He, H. Li, L. Zhang, T. Liu, X. Wang, P. Wang, Z. Liu and G. Cui, *Adv. Energy Mater.*, 2025, 2405766.
28. L. Wu, Z. Jin, X. Xie, F. Lian, J. Lu and W. Wang, *Energy Stor. Mater.*, 2025, **77**, 104167.
29. Y. Jia, Z. Wang, Z. Han, J. Li, M. Zhang, Z. Lao, Y. Han, R. Gao, J. Gao, Z. Zheng, A. Chen, H. Li, R. Mao, K. Tao, J. Li and G. Zhou, *Joule*, 2025, 101878.
30. N. Song, J. Ma, Y. Liang, P. Wang, J. Yuan, S. Xiong, X. Li, J. Feng and B. Xi, *Adv. Mater.*, 2025, 2420588.
31. S. Kim, W.-G. Lim, H. Jung, Y. C. Jeong, C.-Y. Park, S. B. Yang, C. H. Lee, D. Wang, K. Sohn, J. W. Han and J. Lee, *Nat. Commun.*, 2025, **16**, 1649.